Angular dependence of hump-shape Hall Effects for distinguishing between Karplus-Luttinger and Geometrical Origins

Z. S. Lim[1], L. E. Chow[1], A. K. H. Khoo[2], G. J. Omar[1], Z. Luo[1], Z. Zhang[1], H. Yan[1], P. Yang[3], R. Laskowski[2], A. Ariando[1,*]

1. Physics Department, Block S12, #2 Science Drive 3, National University of Singapore 117551

2. Institute of High-Performance Computing (IHPC), A*STAR, Fusionopolis Way, #16-16 Connexis, Singapore 138632

3. Singapore Synchrotron Light Source (SSLS), National University of Singapore, 5 Research Link, Singapore 117603

[*]Email: ariando@nus.edu.sg

ABSTRCT

Among various magnetic thin film heterostructures in solid state Physics, two contrasting mechanisms of the hump-shaped Hall Effects remain ambiguous and debated, namely the overlap of two opposite-signed Karplus-Luttinger Hall-loops associated with inhomogeneous collinear magnetic bubbles with perpendicular anisotropy, or the Geometrical/topological Hall Effect associated with magnetic skyrmions. Their similarity in topology imposes difficulty in discrimination via magnetic imaging. Here, this ambiguity is overcome by the divergence exponent of angle-dependent hump peak fields via magnetic field rotation characterization on several heterostructures. Their difference in sensitivity to in-plane fields reveals that the former mechanism involves higher uniaxial anisotropy than the latter, departing from the pure skyrmion regime described by Ginzburg-Landau framework of triple-$\boldsymbol{q}$ spin-wave superposition. Various materials can be collapsed into a single curve of divergence exponent versus domain wall energy, bridging the crossover of the two mentioned mechanisms.

INTRODUCTION

Theoretical development on Anomalous Hall Effect (AHE) began in 1954 when Karplus and Luttinger (KL)(*1*) formulated the perpendicular electron velocity of the intrinsic mechanism in simple ferromagnetic metals, $v_{\perp} = \frac{1}{i\hbar}\left[\hat{\mathrm{H}}_{\mathrm{soc}}, x_{\perp}\right] = \frac{1}{m^2c^2}\left(\frac{\boldsymbol{M}}{M_s} \times \boldsymbol{\nabla} V\right)$, where spin-orbit coupling (SOC) is the crucial perturbation to the system subjected to an external electric field ($\boldsymbol{\nabla} V$). Later refinement of KL-AHE by McDonald and Nagaosa et al. incorporated the language of k-space Berry curvature $\boldsymbol{\Omega}(\boldsymbol{k})$ to account for anti-crossing in band structures(*2, 3*). Whereas the extrinsic mechanisms involving impurity scattering were account by classifications into skew scattering(*4*) and side-jump(*5, 6*). Until the last two decades, these three sideway electron deflection mechanisms, all of which require SOC on a uniform collinear magnetization ($\boldsymbol{M}$) background, formed the backbone of conventional AHE analyses via $\rho_{xy}^{\mathrm{AHE}}(H) \propto {\rho_{xx}}^{\beta} M(H)$ where $1 \leq \beta \leq 2$ is the extracted exponents(*7*). Then, the abrupt enhancement of non-linear $\rho_{xy}(H,T)$ near Curie temperature (T_C) observed in perovskite manganites(*8, 9*) contrasted with the conventional AHE mechanisms which is expected to diminish with increasing temperature. This motivated extensive theoretical study into the unconventional *subset* of AHE – Geometrical Hall Effect (GHE) emanating from chiral arrangements of magnetic moments in the real-space that form a scalar spin chirality (SSC), viz. a solid angle $\Omega = 2\tan^{-1}\left[\frac{\hat{\boldsymbol{m}}_i \cdot (\hat{\boldsymbol{m}}_j \times \hat{\boldsymbol{m}}_k)}{1 + \hat{\boldsymbol{m}}_i \cdot \hat{\boldsymbol{m}}_j + \hat{\boldsymbol{m}}_j \cdot \hat{\boldsymbol{m}}_k + \hat{\boldsymbol{m}}_k \cdot \hat{\boldsymbol{m}}_i}\right]$ [10]. In the regime where mobile electrons maintain strong and adiabatic exchange interaction with the chiral moments of skyrmions, the Berry phase gained takes the form of Ω which integrates into a pseudo magnetic field $B_{\mathrm{eff}} = \frac{1}{4\pi}\int \boldsymbol{m} \cdot \left(\frac{\partial \boldsymbol{m}}{\partial \mathrm{x}} \times \frac{\partial \boldsymbol{m}}{\partial \mathrm{y}}\right) \mathrm{dxdy}$, resulting $\rho_{xy}^{\mathrm{GHE}}(H) \propto \frac{B_{\mathrm{eff}}}{ne}$ in analogy to the ordinary Lorentz force effect (OHE)(*10, 11*). Theoretically, GHE does not require SOC(*12, 13*) in contrast to the conventional AHE, although the Skyrmion formation may require SOC-induced

Dzyaloshinskii-Moriya Interaction (DMI)(*14, 15*) or crystallographic frustration(*16, 17*). Yet the presence/absence of SOC in electron deflection is difficult to verify in experiments.

Considering the general form of any magnetic texture in cylindrical coordinates (r,ϕ),

$$\boldsymbol{m}(r,\phi) = \begin{bmatrix} \sin(f(r))\cos(Q_v\phi + Q_h) \\ \sin(f(r))\sin(Q_v\phi + Q_h) \\ \cos(f(r)) \end{bmatrix}$$

where $Q_{v,h}$ are the vorticity and helicity(*18*), the radial profile $f(r)$ that varies within the range of $\{0,\pi\}$ is crucial for distinguishing between skyrmions and collinear domains bordered by chiral domain walls (DW), while bubbles are the intermediate form in this crossover. For skyrmions with smoothly varying (sinusoidal) $f(r)$, the mentioned B_{eff} is valid. Furthermore, in the atomic-scale skyrmion-lattice regime with skyrmion size comparable to the atomic lattice parameter and electronic mean free path, a massive Dirac Fermion(*19*) should emerge in the k-space band structure, approaching the Haldane's model(*20*). On the other hand, for collinear bubbles/domains with more step-function-like $f(r)$, one would expect the KL-AHE to contribute significantly (neglecting extrinsic mechanisms for clean samples) since the area ratio of collinear moments to chiral domain walls (DW) becomes large. Besides, for bubbles typically stabilized by dipolar interaction, the $\left(\frac{\partial \boldsymbol{m}}{\partial \mathrm{x}} \times \frac{\partial \boldsymbol{m}}{\partial \mathrm{y}}\right)$ term in B_{eff} is expected to vanish, since the DMI that unifies Q_h is absent, while near-straight DWs (cycloids or helicoids) do not have simultaneous spatial variations in both perpendicular directions(*21*).

Nevertheless, the similarity in topology between skyrmions and collinear bubbles have led to ambiguity and debates in experiments. GHE is usually recognized by its hump-shape $\rho_{xy}^{T}(H_z) \sim \mathcal{L}(H_z)/H_z$ where $\mathcal{L}(H_z) = \coth(H_z) - 1/H_z$ is the Langevin function, and has been observed in various heterostructures of oxide(*22-24*) or magnetically-doped topological insulator (MTI)(*25-28*) bilayers. However, the Hall-humps can also be fitted by overlapping two KL-AHE loops with opposite signs, implying that the material systems in question contain

inhomogeneous collinear domains with opposite k-space Chern number, doubting the existence of skyrmions. Intensive efforts were invested on magnetic imaging to investigate these low-temperature and low-magnetization materials using scanning probe techniques(*29, 30*) and X-ray Photoemission Microscopy (XMCD-PEEM)(*31, 32*). Notably, in single-layer ultrathin $SrRuO_3$ (SRO) with Hall-humps, terrace engineering was used to segregate/coalesce the bubbles along terraces(*33*), to be in favour of the KL-AHE interpretation. On the other hand, the $SrRuO_3/PbTiO_3$ bilayer was found to host a double-$\boldsymbol{q}$ square meron lattice(*34, 35*) which supports the GHE interpretation; likewise for the MTI bilayers which have been understood to stabilize skyrmion-lattice (SkL) via interfacial antiferromagnetic exchange(*36*), similar to the effect of antiferromagnetic frustration in Gd_2PdSi_3(*17*). Hence, a stereotypical viewpoint on Hall-humps should be avoided; yet little emphasis was placed on evaluating the domain wall energy (σ_{DW}) of the textures found(*18, 37*). In this work, by applying magnetic field rotation on contrasting samples, we show that collinear bubble domains and skyrmions can be distinguished by relating the divergence of their Hall-hump peak fields (H_{peak}) to uniaxial anisotropy (K_u). The high sensitivity of skyrmion-hosting samples to in-plane magnetic field is understood from Ginzburg-Landau theory of triple-$\boldsymbol{q}$ spin-wave superposition and supported by micromagnetic simulation. The H_{peak} divergence exponent (γ) from various heterostructures also forms a linear trend with σ_{DW} constituting a continuous crossover from skyrmions to bubbles. Such analyses may potentially become a useful protocol for future disambiguation.

RESULTS

Figures 1a,b and S1a,b present the selected oxide heterostructures for analyses, with fabrication details described in supplementary text. Perovskite SRO thin films are known to have two distinct monoclinic (m-) and tetragonal (t-) phases, with Glazer notations(*38, 39*) of

octahedral rotations/tilts distinguished as $a^-b^+c^-$ and $a^0a^0c^0$ respectively from X-ray Bragg diffractions (XRD) around half-integer HKL-indices(*40*) (Figure S1c). Their KL-AHE loops also differ significantly, i.e. negative- and positive-sign for t-SRO and m-SRO respectively (Figure S1a,b). This difference originates from the opposite signs of *k*-space Chern numbers of different 4d topological t_{2g}-bands, related to the different band occupancy at Fermi level and lower saturation magnetization (M_{sat}) of t-SRO than m-SRO(*23, 33*). In Figure 1a, the "mR_3tR_7" structure formed by ultrathin m-SRO(3uc)/t-SRO(7uc) on $SrTiO_3$(001) exhibits obvious Hall-humps ranging from 3 K to 40 K. It assimilates a z-direction phase separation, intended to represent many recent publications around single-layer SRO including those with xy-plane inhomogeneity(*23, 33, 41, 42*). This is generally valid since an ultrathin t-phase buffer layer is inevitable when SRO is interfaced directly with the cubic $SrTiO_3$(001) surface due to the suppression of octahedral rotations/tilts(*43*), regardless of the growth pressure or substrate's surface termination. Meanwhile, the "mR_5I_{10}" structure in Figure 1b constructed by m-SRO(5uc) on $SrIrO_3$(10uc) also shows large Hall-humps across a wide temperature range of 10-90 K. Here the paramagnetic $SrIrO_3$ is believed to contribute strong SOC and DMI, while functioning as a buffer layer with thickness beyond the octahedral suppression region such that the m-SRO layer above can be proven to be free from phase separation issue. In Figure S2, we provide the magnetic force microscopy (MFM) images of mR_5I_{10} at 20 K and varying out-of-plane magnetic field, proving that magnetic textures akin to SkL indeed exists and reaches maximum density at H_{peak}, agreeing well with the Hall-hump trend.

To shed light on the universality of our subsequent analyses, we included the 8uc and 3uc variants of $Tm_3Fe_5O_{12}$(TmIG) films capped with 2-nm Pt grown on $Gd_3Ga_5O_{12}$(111) substrates, labelled as "P_2T_8" and "P_2T_3", as displayed in Figure 2. TmIG(111) is renowned to be a high-T_C ferrimagnetic insulator with perpendicular anisotropy (PMA) under tensile strain, hence the spin current reflected off the Pt/TmIG interface can detect clear Spin Hall Effect

(SHE) induced square KL-AHE loops(*44-46*) in P_2T_8 and GHE(*47-49*) in P_2T_3 at 300 K. Being slightly different from mR_3tR_7 and mR_5I_{10}, the Hall-humps in P_2T_3 are non-hysteretic and are greatly enhanced around T_C~300 K of the ultrathin (3uc) TmIG, but vanishes at low temperatures. Such phenomenon has been discussed as the chiral fluctuation behaviour(*24*) with a proximity-magnetized Pt in its carrier localization regime, and exhibits a power-law enhancement around the 2nd-order transition temperature(*50*).

The main focus of this work is the investigation of Hall effects with rotation of magnetic field ($\rho_{xy}(H_{\text{total}}, \theta)$) from out-of-plane ($H||z$ at θ=0°) approaching in-plane ($H||x,y$ at θ→90°), at 20 K for mR_3tR_7 and mR_5I_{10} and 300 K for P_2T_8 and P_2T_3. The measurement schematic is illustrated in Figure 1c, presented in total field, $H_{\text{total}} = \sqrt{{H_z}^2 + {H_{x,y}}^2}$, implying the field sweep is in the 1st and 3rd quadrants. Notably in Figure 1d, the H_{peak} of mR_3tR_7 exhibits fast divergence with increasing θ (left panel), which can be fitted with a phenomenological $H_{\text{peak}} \propto 1/\cos^{\gamma}(\theta)$ to obtain γ=0.76 (Figure 1f). Note that the γ→1 limit implies a high K_u sample with zero contribution from in-plane fields since the out-of-plane magnetization component (M_z) is responsible for the KL-AHE. It is then instructive to decompose the Hall data of mR_3tR_7 at θ=0° into two KL-AHE loops of opposite signs via $\rho_{xy}(H,\theta) = \sum_{i=1,2} A_i \left\{\coth\left[B_i\left(H - \frac{H_{C,i}(\theta=0)}{\cos^{\gamma}(\theta)}\right)\right] - \left[B_i\left(H - \frac{H_{C,i}(\theta=0)}{\cos^{\gamma}(\theta)}\right)\right]^{-1}\right\}$ where and A_i and B_i are coefficients, and the two coercive fields ($H_{C1,2}$) delimit the range where the Hall humps would emerge. Such θ-dependent Hall analysis, albeit unprecedented, supports that mR_3tR_7 hosts inhomogeneous bubble-like domains at intermediate fields in agreement to reference (*33*). Likewise, the KL-AHE of P_2T_8 in Figure 2a,c also showed an obvious divergence of $H_C \propto 1/\cos^{0.45}(\theta)$. In contrast, the H_{peak} of mR_5I_{10} and P_2T_3 were found to be independent of θ with extracted γ~0.06 and 0.03 while the

hump magnitudes ($\Delta\rho_{xy}$) also diminished at large θ-angles, as shown in Figure 1e,f and Figure 2d-f respectively.

To understand the large divergence reflected by γ=0.74 and 0.45 in mR_3tR_7 and P_2T_8 respectively, we further resolve the out-of-plane (H_z) and in-plane ($H_{x,y}$) field components during measurements. The Hall measurements were done by sweeping H_z with a constant $H_{x,y}$, while the H_{total} vector is rotating in the 1st and 2nd quadrants or the 4th and 3rd quadrants for a particular $\rho_{xy}(H_z, H_{x,y})$ loop (schematic in Figure 3e). In Figure 3a,b, a linear shift of z-component peak field $H_{peak,z}$ towards left and right sides can be observed in mR_3tR_7 with varying $H_{x,y}$ in the range of ±3 T. Notably, the loop width demarcated by the $\pm H_{peak,z}$ stayed nearly constant, thus the $\mp H_{peak,z}$ opposite to the shift direction can reach near-zero at large $\pm H_{x,y}$. Similar shift in z-component ($H_{C,z}$) can be observed in P_2T_8 as shown in Figure S3a,b with additional discussion in supplementary text. Such loop-shift can be understood as a destabilization of the $\pm M_z$ by the in-plane magnetic field, ie.: easier (harder) to switch M_z downwards (upward) assisted by a positive $H_{x,y}$, and vice versa. Hence, the horizontal expansion of $\rho_{xy}(H_{total}, \theta)$ and the horizontal shift of $\rho_{xy}(H_z, H_{x,y})$ observed in the two field-rotation methods are equivalent, since the former involving field-sweep in the 1st-3rd (or 4th-2nd) quadrants causes increasing switching difficulty to both polarity of $\pm M_z$. The data inter-conversion in these two methods can be seen in supplementary Figure S4a,b. Note that a broken parity symmetry exists where a right-shift of $\rho_{xy}(H_z, H_{x,y})$ loop is always observed for $+H_{x,y}$ and vice versa. This can be understood by the large polar angle of SRO's easy axis tilting up to 45° away from [001] due to a competition between in-plane and out-of-plane anisotropies(*40, 51*) (Figure 3c); and is also similar to P_2T_8 (Figure S3a). Such broken parity is confirmed to be irrelevant to the spin-orbit torque (SOT), since neither of loop shift direction reversal upon $J_x \Leftrightarrow J_{-x}$ nor loop shift vanish with changing $H_x \Rightarrow H_y$ was observed. To be consistent with mR_5I_{10}, we limited our investigation to magnetostatic at low current densities to avoid magnetization

dynamics and Joule heating; however, the loop shift enhancement can be expected if larger J_x up to 10^{10} A/m^2 is sourced, as exemplified by P_2T_8 (Figure S4c). Conversely, under the same "resolved field-components" method, mR_5I_{10} (Figure 3d) and P_2T_3 (Figure S3c) showed stationary $H_{z,\text{peak}}$ without left/right shifting but fast-vanishing Hall-humps with varying $H_{x,y}$. Hence, it is convincing to rule out the existence of inhomogeneous collinear magnetic bubbles in mR_5I_{10} and P_2T_3.

SIMULATIONS

For comparison with properties of Néel-type magnetic skyrmions, we first evaluated the interfacial DMI values of mR_3tR_7 and mR_5I_{10} via Density Functional Theory (DFT) calculations, by using the "two-slab" structural models as displayed in Figure 4a,b. The mismatches in octahedral tilt across the interfaces are accounted, i.e. SRO($a^-b^+c^0$)/SRO($a^0b^0c^0$) for mR_3tR_7 and SRO($a^-b^+c^0$)/SIO($a^+b^0c^0$) for mR_5I_{10}, as deduced from half-integer XRD data (Figure S1c). The obtained diffraction peaks agree qualitatively with the expected concepts of bond length variation(*52*) and strain relaxation as discussed in the supplementary text, although the quantitative rotation angles with thickness variation cannot be determined at present. As shown in Figure 4c,d, due to the presence of heavy element (Ir^{4+}), a significantly higher interfacial DMI of 0.76 mJ/m^2 was obtained in mR_5I_{10} as compared to merely 0.071 mJ/m^2 in mR_3tR_7, contrasting their likelihood in hosting skyrmions. Hence, MUMAX^3 micromagnetic simulations(*53*) were performed on mR_5I_{10} to compute the topological charge density (*TCD*) = $\frac{1}{4\pi}\boldsymbol{m}\cdot\left(\frac{\partial \boldsymbol{m}}{\partial x}\times\frac{\partial \boldsymbol{m}}{\partial y}\right)$, by using the DMI and other parameters extracted from magnetometry (Figure S5b) as inputs, and incorporating magnetic field rotation $B_{\text{ext}} = B_{\text{total}}[\sin\theta, 0, \cos\theta]$ (details in supplementary text). In Figures 4e, the $TCD(H_{\text{total}}, \theta)$ mappings shows that the peak fields corresponding to the densest SkL remain non-diverging, in good agreement to the $\rho_{xy}(H_{\text{total}}, \theta)$ trend shown in Figure 1e. The similar observation was obtained in P_2T_3 by using

parameters extracted from various references (Figure S3d). This can be understood by considering the Ginzburg-Landau framework for triple-$\boldsymbol{q}$ spin-waves superposition. It is well-known that a trio of cycloidal spin-waves that can be described by $\boldsymbol{m}_i = \sum_{i=1,2,3}[\hat{\boldsymbol{z}}\cos(\boldsymbol{q}_i \cdot \boldsymbol{r}) \pm \boldsymbol{q}_i \sin(\boldsymbol{q}_i \cdot \boldsymbol{r})]$ would create a two-dimensional (2D) hexagonal-close-packed Néel-SkL stabilized by a small H_z, where $\boldsymbol{r} = [x, y, z]$, and wave vectors $\boldsymbol{q}_i = \left[\cos\left(\frac{2\pi i}{3}\right), \sin\left(\frac{2\pi i}{3}\right), 0\right]$. Likewise, helicoidal spin-waves with $\boldsymbol{m}_i = \sum_{i=1,2,3}[\hat{\boldsymbol{z}}\cos(\boldsymbol{q}_i \cdot \boldsymbol{r}) \pm (\hat{\boldsymbol{z}} \times \boldsymbol{q}_i)\sin(\boldsymbol{q}_i \cdot \boldsymbol{r})]$ would create a 2D Bloch-type SkL. Then, application of H_x would cause $\boldsymbol{m}$ to precess around H_x, hence the dominant single-$\boldsymbol{q}$ is perpendicular (parallel) to $\boldsymbol{H}_x$ for the Néel-type (Bloch-type) case(*54-56*). Due to this vulnerability of SkLs subjected to in-plane fields, the total field of peak *TCD* should be almost θ-independent before skyrmion annihilation. Figure 5a illustrates that the variation of K_u within one order-of-magnitude in the simulation creates gentle *TCD* peak-field divergence around γ~0, hence is unable to produce large divergence like that of mR_3tR_7. These simulations do not lose generality and are invariant under the change of H_x to H_y, or interface to bulk DMI for Néel- to Bloch-type skyrmions in such thin film regime. The observations above validate the grouping of Hall-humps of mR_3tR_7 and P_2T_8 as indication of collinear bubble domains, while mR_5I_{10} and P_2T_3 can be categorized as hosting skyrmions.

DISCUSSION

Theoretical understanding has established that the subtle difference between trivial domains and topological textures lies at the domain wall energy $\sigma_{DW} = 4\sqrt{A_{ex}K_{eff}} - \pi D$ which is positive for trivial and negative for topological(*57*), where A_{ex} is the exchange stiffness and $K_{eff} = K_u + \mu_o {M_{sat}}^2/2$ taking account of dipolar interaction. The second term (πD) may originate from SOC-induced DMI, or effectively from honeycomb lattice or antiferromagnetic frustration. In the intermediate regime where $4\sqrt{A_{ex}K_u} < \pi D < 4\sqrt{A_{ex}K_{eff}}$, sparsely

separated individual collinear bubbles can be found which is applicable for many metallic multilayer stacks explored to date, yet they are actually different from the SkL formed at the condition of $4\sqrt{A_{ex}K_{eff}} < \pi D$. Here, we repeated the total field rotation method for a plethora of other oxide heterostructures as summarized in Figure 5b with data listed in Table S2, presuming that γ is a good quantification parameter for Hall-hump shift due to in-plane magnetic field, and represents the likelihood of trivial domains. Hence, a linear relationship between the scaling exponent γ and σ_{DW} was obtained. In particular, the $SrRuO_3/BaTiO_3$ bilayer and superlattice heterostructures can be found at the intermediate regime of the plot, while their magnetometry and γ extractions data are presented in supplementary Figure S5c-f. Such systems might be potentially ambiguous since the interfacial DMI was calculated by first-principle to be quite large (~0.84 mJ/m^2)(*58*), yet a consensus about the magnetic texture identity corresponding to the Hall-humps has not been reached in imaging(*34*). Here, the observed γ~0.6 may likely be an inspiring bridge to understand that the $SrRuO_3/BaTiO_3$ heterostructures are in the mixed trivial bubbles and skyrmions regime, since its tetragonal crystal structure contributes a large K_u. Without the in-plane field schemes to scrutinize textures movement, expansion or annihilation, a general imaging technique would still be difficult to reach a satisfactory conclusion for such mixed state. One may also envision a reducing trend of threshold current density of moving the skyrmions or bubble domains by SOT with reducing γ, consistent to the idea of topological protection and evasion of impurity pinning(*59*), but is currently out-of-scope in this work.

In conclusions, the gradual crossover of Hall-humps with origin from KL-AHE to GHE has been elucidated by observing the response of Hall-humps to in-plane magnetic fields to distinguish the behaviours of trivial domains and genuine magnetic skyrmions. This method holds promise as an indispensable protocol in complementing magnetic imaging techniques for future development of skyrmion-based topological spintronics and stochastic computing.

MATERIALS AND METHODS

For all-oxide heterostructures incluing mR_3tR_7, mR_5I_{10}, $B1_2S_8$ and $(B_4S_4)_{x4}$-SL, the STO(001) substrates' surface were etched by buffered-HF solutions and annealed at 950ºC for 1.5 hours to achieve single TiO_2-termination. Hall-bars were defined by depositing insulating amorphous AlN film with thickness ~200 nm on the STO(001) substrates, followed by photolithography and lift-off. Such Hall-bars fabrication before crystal film growth has the advantages of avoiding ion milling that might induce unwanted oxygen vacancies, water leaching problem(*60*), or chemical doping(*61*) during photolithography. Single-crystalline m-phase SRO and SIO films were grown on the exposed STO surface at 660ºC and 750ºC temperatures respectively and oxygen pressure PO_2=100 mTorr in a Pulsed Laser Deposition (PLD) system, hence the m-SRO thick film (34uc) shows negative-sign KL-AHE (Figure S1a). Whereas the t-phase SRO was grown at 660ºC and PO_2=15 mTorr, showing positive-sign KL-AHE (Figure S1b). The $B_{12}S_8$ was constructed by 8.5uc of SRO film grown on STO(001) at 660ºC and PO_2=100 mTorr, followed by 12uc BTO at PO_2=2 mTorr and same temperature. The extra 0.5uc of SRO is to account for termination change from TiO_2 to SrO at the first uc. Whereas the $(B_4S_4)_{x4}$-SL is actually a superlattice of $[SRO(4uc)\ on\ BTO(4uc)]_{x4}$ capped with a final 4uc BTO, constructed by alternating BTO at PO_2=10 mTorr and SRO at PO_2=50 mTorr at a common temperature 700ºC. The materials deposited on AlN are amorphous and insulating. For structures P_2T_8 and P_2T_3, the GGG(111) substrates which were annealed at 1000ºC and 6 hours. Then, crystalline TmIG films were grown directly on the substrates at 700ºC and PO_2=15 mTorr, before *in-situ* transfer to a sputtering chamber for amorphous Pt capping at room temperature at low speed of 1.62 nm/min to ensure high quality interface. Finally, Hall-bars were defined by photolithography and ion beam milling, since the AlN pre-deposited Hall-bars do not work in cases with Pt capping which is still conducting on amorphous AlN. All Hall-bars are 200-μm long and 20-μm wide. All films have minimal surface roughness of ~rms.

0.2 nm without island growth (step-flow and layer-by-layer for SRO and SIO respectively), so that high quality interfaces are ensured. The final topography of all samples were checked by ParkSystems model NX10 Atomic Force Microscope (AFM). Electrical measurements were done in a Quantum Design (QD) Physical Properties Measurement System (PPMS-6000) equipped with a rotator attachment, while and magnetometry was measured in a QD Superconducting Quantum Interference Device (SQUID) Vibrating Sample Magnetometery (VSM). The PPMS and SQUID-VSM can cool samples down to 2 K and apply magnetic field up to +/-9 T and +/-7 T respectively. In PPMS, before measurements on P_2T_8 with low $\mu_o H_C$ of only ~2.2 mT, the magnetic field was first set to 1 T before ramping down to zero in the oscillating mode to remove any residual field due to vortices in the superconducting coil of PPMS. The "total field rotation measurements" for $\rho_{xy}(H_{\text{total}}, \theta)$ were done with pseudoAC currents to eliminate thermal noise, while the "resolved field components measurements" for $\rho_{xy}(H_z, H_x)$ were done with DC currents supplied by a Keithley 2400 sourcemeter. X-ray diffraction was measured at the XDD beamline of Singapore Synchrotron Light Source (SSLS). Magnetic imaging by change in frequency (Δf) was performed by the low-temperature MFM mode of AttoAFM1, which is capable of cooling down to 1.5 K and applying magnetic field up to +/-8 T. Extra details are given in the *Supplementary Materials.*

ACKNOWLEDGEMENT

This work is supported by the Agency for Science, Technology and Research (A*STAR) under its Advanced Manufacturing and Engineering (AME) Individual Research Grant (IRG) (A1983c0034), the National University of Singapore (NUS) Academic Research Fund (A-0004196-00-00), and the Singapore National Research Foundation (NRF) under the Competitive Research Programs (CRP Award No. NRF-CRP15-2015-01). Dr. P. Yang is supported by SSLS via NUS Core Support C-380-003-003-001. The authors would also like to

acknowledge the Singapore Synchrotron Light Source (SSLS) for providing the facilities necessary for conducting the research. The SSLS is a National Research Infrastructure under the National Research Foundation Singapore. Special thanks also go to Max Hirschberger for an insightful short discussion.

AUTHOR CONTRIBUTIONS

A. A. provided all necessary laboratory facilities. Z. S. L. and A.A. constructed the idea and experiment plans. Z. S. L., L. E. C. and G. J. O. grew the oxide films in a PLD system. A. K. H. K. and R. L. performed the DFT calculations. Z. S. L., L. E. C., G. J. O., Z. L, Z. Z. and H. Y. participated in Hall measurements, data analyses and discussions. P. Y. provided valuable experience and guidance at the SSLS-XDD beamline.

COMPETING INTERESTS

All authors declare no financial or non-financial competing interests.

DATA AND MATERIALS AVAILABILITY

The datasets used and/or analysed during the current study are available from the corresponding author upon reasonable request.

REFERENCES

1. R. Karplus, J. M. Luttinger, Hall Effect in Ferromagnetics. *Physical Review* **95**, 1154-1160 (1954).
2. T. Jungwirth, Q. Niu, A. H. MacDonald, Anomalous Hall Effect in Ferromagnetic Semiconductors. *Phys. Rev. Lett.* **88**, 207208 (2002).
3. M. Onoda, N. Nagaosa, Topological Nature of Anomalous Hall Effect in Ferromagnets. *J. Phys. Soc. Jpn.* **71**, 19-22 (2002).
4. J. Smit, The spontaneous hall effect in ferromagnetics II. *Phy* **24**, 39-51 (1958).
5. L. Berger, Side-Jump Mechanism for the Hall Effect of Ferromagnets. *Phys. Rev. B* **2**, 4559-4566 (1970).
6. P. Nozières, C. Lewiner, A simple theory of the anomalous hall effect in semiconductors. *J. Phys. (Paris)* **34**, 901-915 (1973).
7. N. Nagaosa, J. Sinova, S. Onoda, A. H. MacDonald, N. P. Ong, Anomalous Hall effect. *Reviews of Modern Physics* **82**, 1539-1592 (2010).
8. S. H. Chun, M. B. Salamon, Y. Lyanda-Geller, P. M. Goldbart, P. D. Han, Magnetotransport in Manganites and the Role of Quantal Phases: Theory and Experiment. *Phys. Rev. Lett.* **84**, 757-760 (2000).
9. J. Ye, Y. B. Kim, A. J. Millis, B. I. Shraiman, P. Majumdar, Z. Tešanović, Berry Phase Theory of the Anomalous Hall Effect: Application to Colossal Magnetoresistance Manganites. *Phys. Rev. Lett.* **83**, 3737-3740 (1999).
10. K. Everschor-Sitte, M. Sitte, Real-space Berry phases: Skyrmion soccer (invited). *Journal of Applied Physics* **115**, 172602 (2014).
11. P. Bruno, V. K. Dugaev, M. Taillefumier, Topological Hall Effect and Berry Phase in Magnetic Nanostructures. *Phys. Rev. Lett.* **93**, 096806 (2004).
12. Y. Zhang, Y. Sun, H. Yang, J. Železný, S. P. P. Parkin, C. Felser, B. Yan, Strong anisotropic anomalous Hall effect and spin Hall effect in the chiral antiferromagnetic compounds Mn_3X, (X=Ge, Sn, Ga, Ir, Rh, and Pt). *Phys. Rev. B* **95**, 075128 (2017).
13. H. Ishizuka, N. Nagaosa, Spin chirality induced skew scattering and anomalous Hall effect in chiral magnets. *Sci. Adv.* **4**, eaap9962 (2018).
14. I. Dzyaloshinsky, A thermodynamic theory of "weak" ferromagnetism of antiferromagnetics. *Journal of Physics and Chemistry of Solids* **4**, 241-255 (1958).
15. T. Moriya, Anisotropic Superexchange Interaction and Weak Ferromagnetism. *Physical Review* **120**, 91-98 (1960).
16. A. O. Leonov, M. Mostovoy, Multiply periodic states and isolated skyrmions in an anisotropic frustrated magnet. *Nat. Commun.* **6**, 8275 (2015).
17. T. Kurumaji, T. Nakajima, M. Hirschberger, A. Kikkawa, Y. Yamasaki, H. Sagayama, H. Nakao, Y. Taguchi, T.-h. Arima, Y. Tokura, Skyrmion lattice with a giant topological Hall effect in a frustrated triangular-lattice magnet. *Science* **365**, 914-918 (2019).
18. N. Nagaosa, Y. Tokura, Topological properties and dynamics of magnetic skyrmions. *Nat. Nanotechnol.* **8**, 899 (2013).
19. K. Hamamoto, M. Ezawa, N. Nagaosa, Quantized topological Hall effect in skyrmion crystal. *Phys. Rev. B* **92**, 115417 (2015).
20. F. D. M. Haldane, Model for a Quantum Hall Effect without Landau Levels: Condensed-Matter Realization of the "Parity Anomaly". *Physical Review Letters* **61**, 2015-2018 (1988).

21. F. R. Lux, F. Freimuth, S. Blügel, Y. Mokrousov, Engineering chiral and topological orbital magnetism of domain walls and skyrmions. *Communications Physics* **1**, 60 (2018).
22. J. Matsuno, N. Ogawa, K. Yasuda, F. Kagawa, W. Koshibae, N. Nagaosa, Y. Tokura, M. Kawasaki, Interface-driven topological Hall effect in $SrRuO_3$-$SrIrO_3$ bilayer. *Sci. Adv.* **2**, e1600304 (2016).
23. D. J. Groenendijk, C. Autieri, T. C. van Thiel, W. Brzezicki, J. R. Hortensius, D. Afanasiev, N. Gauquelin, P. Barone, K. H. W. van den Bos, S. van Aert, J. Verbeeck, A. Filippetti, S. Picozzi, M. Cuoco, A. D. Caviglia, Berry phase engineering at oxide interfaces. *Phys. Rev. Res.* **2**, 023404 (2020).
24. W. Wang, M. W. Daniels, Z. Liao, Y. Zhao, J. Wang, G. Koster, G. Rijnders, C.-Z. Chang, D. Xiao, W. Wu, Spin chirality fluctuation in two-dimensional ferromagnets with perpendicular magnetic anisotropy. *Nat. Mater.* **18**, 1054-1059 (2019).
25. K. Yasuda, R. Wakatsuki, T. Morimoto, R. Yoshimi, A. Tsukazaki, K. S. Takahashi, M. Ezawa, M. Kawasaki, N. Nagaosa, Y. Tokura, Geometric Hall effects in topological insulator heterostructures. *Nat. Phys.* **12**, 555-559 (2016).
26. C. Liu, Y. Zang, W. Ruan, Y. Gong, K. He, X. Ma, Q.-K. Xue, Y. Wang, Dimensional Crossover-Induced Topological Hall Effect in a Magnetic Topological Insulator. *Phys. Rev. Lett.* **119**, 176809 (2017).
27. K. M. Fijalkowski, M. Hartl, M. Winnerlein, P. Mandal, S. Schreyeck, K. Brunner, C. Gould, L. W. Molenkamp, Coexistence of Surface and Bulk Ferromagnetism Mimics Skyrmion Hall Effect in a Topological Insulator. *Phys. Rev. X* **10**, 011012 (2020).
28. J. Jiang, D. Xiao, F. Wang, J.-H. Shin, D. Andreoli, J. Zhang, R. Xiao, Y.-F. Zhao, M. Kayyalha, L. Zhang, K. Wang, J. Zang, C. Liu, N. Samarth, M. H. W. Chan, C.-Z. Chang, Concurrence of quantum anomalous Hall and topological Hall effects in magnetic topological insulator sandwich heterostructures. *Nat. Mater.*, (2020).
29. L. Vistoli, W. Wang, A. Sander, Q. Zhu, B. Casals, R. Cichelero, A. Barthélémy, S. Fusil, G. Herranz, S. Valencia, R. Abrudan, E. Weschke, K. Nakazawa, H. Kohno, J. Santamaria, W. Wu, V. Garcia, M. Bibes, Giant topological Hall effect in correlated oxide thin films. *Nat. Phys.* **15**, 67-72 (2019).
30. K.-Y. Meng, A. S. Ahmed, M. Baćani, A.-O. Mandru, X. Zhao, N. Bagués, B. D. Esser, J. Flores, D. W. McComb, H. J. Hug, F. Yang, Observation of Nanoscale Skyrmions in $SrIrO_3$/$SrRuO_3$ Bilayers. *Nano Lett.* **19**, 3169-3175 (2019).
31. E. Skoropata, J. Nichols, J. M. Ok, R. V. Chopdekar, E. S. Choi, A. Rastogi, C. Sohn, X. Gao, S. Yoon, T. Farmer, R. D. Desautels, Y. Choi, D. Haskel, J. W. Freeland, S. Okamoto, M. Brahlek, H. N. Lee, Interfacial tuning of chiral magnetic interactions for large topological Hall effects in $LaMnO_3$/$SrIrO_3$ heterostructures. *Sci. Adv.* **6**, eaaz3902 (2020).
32. S. Zhang, F. Kronast, G. van der Laan, T. Hesjedal, Real-Space Observation of Skyrmionium in a Ferromagnet-Magnetic Topological Insulator Heterostructure. *Nano Lett.* **18**, 1057-1063 (2018).
33. L. Wang, Q. Feng, H. G. Lee, E. K. Ko, Q. Lu, T. W. Noh, Controllable Thickness Inhomogeneity and Berry Curvature Engineering of Anomalous Hall Effect in $SrRuO_3$ Ultrathin Films. *Nano Lett.* **20**, 2468-2477 (2020).
34. S. D. Seddon, D. E. Dogaru, S. J. R. Holt, D. Rusu, J. J. P. Peters, A. M. Sanchez, M. Alexe, Real-space observation of ferroelectrically induced magnetic spin crystal in $SrRuO_3$. *Nat. Commun.* **12**, 2007 (2021).
35. Y. Tokura, N. Kanazawa, Magnetic Skyrmion Materials. *Chemical Reviews* **121**, 2857-2897 (2021).

36. Q. L. He, G. Yin, A. J. Grutter, L. Pan, X. Che, G. Yu, D. A. Gilbert, S. M. Disseler, Y. Liu, P. Shafer, B. Zhang, Y. Wu, B. J. Kirby, E. Arenholz, R. K. Lake, X. Han, K. L. Wang, Exchange-biasing topological charges by antiferromagnetism. *Nat. Commun.* **9**, 2767 (2018).
37. X. Zhang, Y. Zhou, K. Mee Song, T.-E. Park, J. Xia, M. Ezawa, X. Liu, W. Zhao, G. Zhao, S. Woo, Skyrmion-electronics: writing, deleting, reading and processing magnetic skyrmions toward spintronic applications. *J. Phys.: Condens. Matter* **32**, 143001 (2020).
38. A. M. Glazer, Simple ways of determining perovskite structures. *AcCrA* **31**, 756-762 (1975).
39. A. M. Glazer, The classification of tilted octahedra in perovskites. *AcCrB* **28**, 3384-3392 (1972).
40. W. Lu, P. Yang, W. D. Song, G. M. Chow, J. S. Chen, Control of oxygen octahedral rotations and physical properties in $SrRuO_3$ films. *Phys. Rev. B* **88**, 214115 (2013).
41. Q. Qin, L. Liu, W. Lin, X. Shu, Q. Xie, Z. Lim, C. Li, S. He, G. M. Chow, J. Chen, Emergence of Topological Hall Effect in a $SrRuO_3$ Single Layer. *Adv. Mater.* **31**, 1807008 (2019).
42. D. Kan, T. Moriyama, K. Kobayashi, Y. Shimakawa, Alternative to the topological interpretation of the transverse resistivity anomalies in $SrRuO_3$. *Phys. Rev. B* **98**, 180408 (2018).
43. Z. Liao, M. Huijben, Z. Zhong, N. Gauquelin, S. Macke, R. J. Green, S. Van Aert, J. Verbeeck, G. Van Tendeloo, K. Held, G. A. Sawatzky, G. Koster, G. Rijnders, Controlled lateral anisotropy in correlated manganite heterostructures by interface-engineered oxygen octahedral coupling. *Nat. Mater.* **15**, 425-431 (2016).
44. C. O. Avci, A. Quindeau, C.-F. Pai, M. Mann, L. Caretta, A. S. Tang, M. C. Onbasli, C. A. Ross, G. S. D. Beach, Current-induced switching in a magnetic insulator. *Nat. Mater.* **16**, 309-314 (2017).
45. C. O. Avci, E. Rosenberg, L. Caretta, F. Büttner, M. Mann, C. Marcus, D. Bono, C. A. Ross, G. S. D. Beach, Interface-driven chiral magnetism and current-driven domain walls in insulating magnetic garnets. *Nature Nanotechnology* **14**, 561-566 (2019).
46. S. Vélez, J. Schaab, M. S. Wörnle, M. Müller, E. Gradauskaite, P. Welter, C. Gutgsell, C. Nistor, C. L. Degen, M. Trassin, M. Fiebig, P. Gambardella, High-speed domain wall racetracks in a magnetic insulator. *Nat. Commun.* **10**, 4750 (2019).
47. A. S. Ahmed, A. J. Lee, N. Bagués, B. A. McCullian, A. M. A. Thabt, A. Perrine, P.-K. Wu, J. R. Rowland, M. Randeria, P. C. Hammel, D. W. McComb, F. Yang, Spin-Hall Topological Hall Effect in Highly Tunable Pt/Ferrimagnetic-Insulator Bilayers. *Nano Lett.* **19**, 5683-5688 (2019).
48. Q. Shao, Y. Liu, G. Yu, S. K. Kim, X. Che, C. Tang, Q. L. He, Y. Tserkovnyak, J. Shi, K. L. Wang, Topological Hall effect at above room temperature in heterostructures composed of a magnetic insulator and a heavy metal. *Nat. Electron.* **2**, 182-186 (2019).
49. A. J. Lee, A. S. Ahmed, J. Flores, S. Guo, B. Wang, N. Bagués, D. W. McComb, F. Yang, Probing the Source of the Interfacial Dzyaloshinskii-Moriya Interaction Responsible for the Topological Hall Effect in Metal/$Tm_3Fe_5O_{12}$ bilayers. *Phys. Rev. Lett.* **124**, 107201 (2020).
50. M. Raju, A. P. Petrović, A. Yagil, K. S. Denisov, N. K. Duong, B. Göbel, E. Şaşıoğlu, O. M. Auslaender, I. Mertig, I. V. Rozhansky, C. Panagopoulos, Colossal topological Hall effect at the transition between isolated and lattice-phase interfacial skyrmions. *Nat. Commun.* **12**, 2758 (2021).

51. L. Liu, Q. Qin, W. Lin, C. Li, Q. Xie, S. He, X. Shu, C. Zhou, Z. Lim, J. Yu, W. Lu, M. Li, X. Yan, S. J. Pennycook, J. Chen, Current-induced magnetization switching in all-oxide heterostructures. *Nat. Nanotechnol.* **14**, 939-944 (2019).
52. T. C. van Thiel, J. Fowlie, C. Autieri, N. Manca, M. Šiškins, D. Afanasiev, S. Gariglio, A. D. Caviglia, Coupling Lattice Instabilities Across the Interface in Ultrathin Oxide Heterostructures. *ACS Materials Letters* **2**, 389-394 (2020).
53. A. Vansteenkiste, J. Leliaert, M. Dvornik, M. Helsen, F. Garcia-Sanchez, B. V. Waeyenberge, The design and verification of MuMax3. *AIP Advances* **4**, 107133 (2014).
54. A. O. Leonov, I. Kézsmárki, Skyrmion robustness in noncentrosymmetric magnets with axial symmetry: The role of anisotropy and tilted magnetic fields. *Phys. Rev. B* **96**, 214413 (2017).
55. X. Wan, Y. Hu, B. Wang, Controlling stability and emergent rotation of the skyrmion crystal in thin films of helimagnets via tilted magnetic field. *Phys. Rev. B* **99**, 180406 (2019).
56. S. Zhang, J. Zhang, Y. Wen, E. M. Chudnovsky, X. Zhang, Determination of chirality and density control of Néel-type skyrmions with in-plane magnetic field. *Communications Physics* **1**, 36 (2018).
57. A. Bogdanov, A. Hubert, Thermodynamically stable magnetic vortex states in magnetic crystals. *Journal of Magnetism and Magnetic Materials* **138**, 255-269 (1994).
58. L. Wang, Q. Feng, Y. Kim, R. Kim, K. H. Lee, S. D. Pollard, Y. J. Shin, H. Zhou, W. Peng, D. Lee, W. Meng, H. Yang, J. H. Han, M. Kim, Q. Lu, T. W. Noh, Ferroelectrically tunable magnetic skyrmions in ultrathin oxide heterostructures. *Nat. Mater.* **17**, 1087-1094 (2018).
59. J. Iwasaki, M. Mochizuki, N. Nagaosa, Universal current-velocity relation of skyrmion motion in chiral magnets. *Nat. Commun.* **4**, 1463 (2013).
60. G. Kimbell, C. Kim, W. Wu, M. Cuoco, J. W. A. Robinson, Challenges in identifying chiral spin textures via the topological Hall effect. *Communications Materials* **3**, 19 (2022).
61. Z. Li, S. Shen, Z. Tian, K. Hwangbo, M. Wang, Y. Wang, F. M. Bartram, L. He, Y. Lyu, Y. Dong, G. Wan, H. Li, N. Lu, J. Zang, H. Zhou, E. Arenholz, Q. He, L. Yang, W. Luo, P. Yu, Reversible manipulation of the magnetic state in $SrRuO_3$ through electric-field controlled proton evolution. *Nat. Commun.* **11**, 184 (2020).
62. L. Caretta, E. Rosenberg, F. Büttner, T. Fakhrul, P. Gargiani, M. Valvidares, Z. Chen, P. Reddy, D. A. Muller, C. A. Ross, G. S. D. Beach, Interfacial Dzyaloshinskii-Moriya interaction arising from rare-earth orbital magnetism in insulating magnetic oxides. *Nat. Commun.* **11**, 1090 (2020).
63. C. Tang, P. Sellappan, Y. Liu, Y. Xu, J. E. Garay, J. Shi, Anomalous Hall hysteresis in $Tm_3Fe_5O_{12}$/Pt with strain-induced perpendicular magnetic anisotropy. *Phys. Rev. B* **94**, 140403 (2016).
64. Z. S. Lim, C. Li, Z. Huang, X. Chi, J. Zhou, S. Zeng, G. J. Omar, Y. P. Feng, A. Rusydi, S. J. Pennycook, T. Venkatesan, A. Ariando, Emergent Topological Hall Effect at a Charge-Transfer Interface. *Small* **16**, 2004683 (2020).

FIGURES

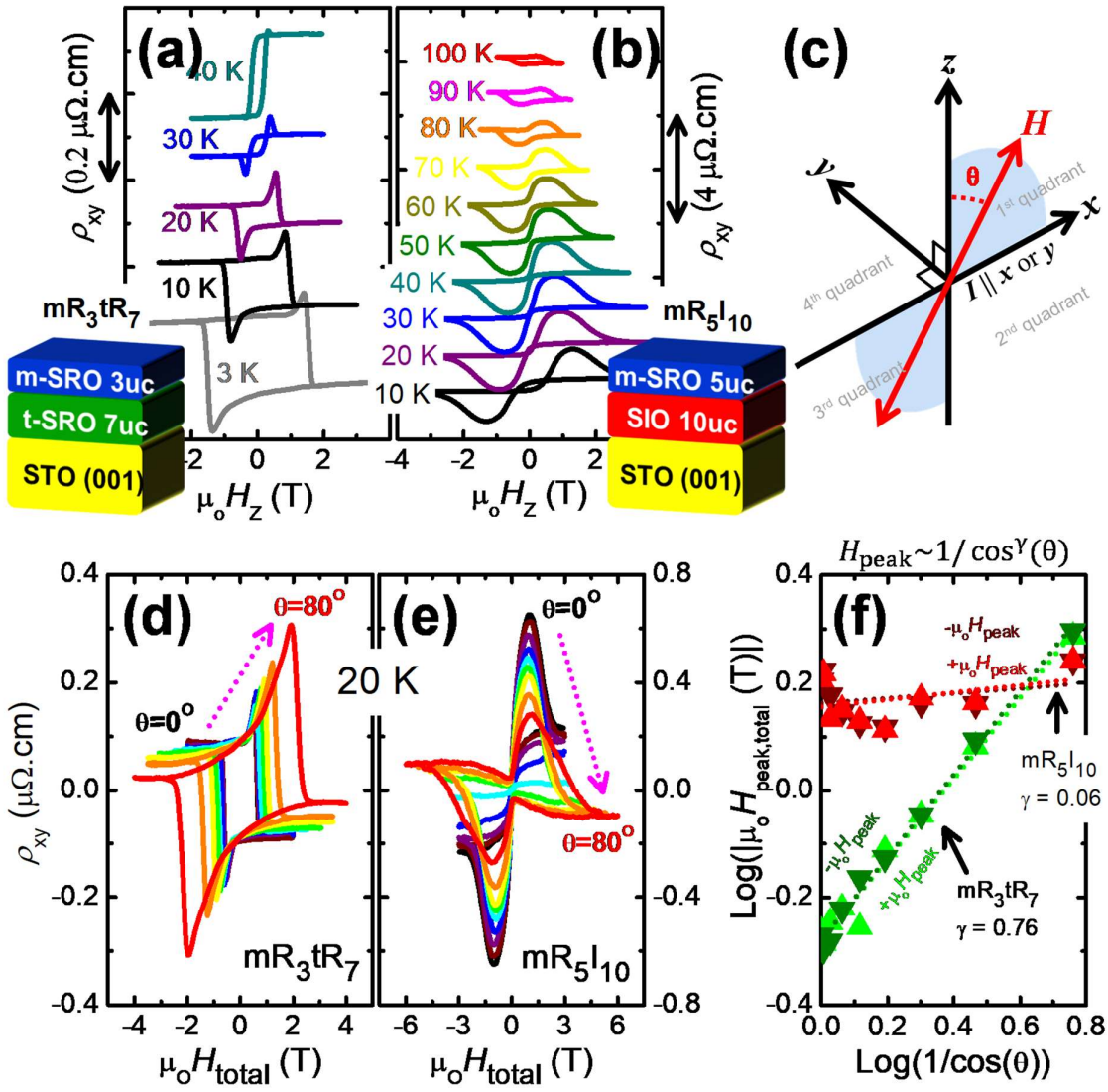

Figure 1: Temperature-dependent Hall loops of **(a)** mR_3tR_7 and **(b)** mR_5I_{10} on STO(001) substrates with obvious Hall-humps. All OHE components were removed by linear background substraction and loops are shifted vertically. **(c)** Schematic of the total field rotation $\rho_{xy}(H_{\text{total}}, \theta)$ measurements, yielding data for **(d)** mR_3tR_7 and **(e)** mR_5I_{10} in the xz-plane at 20 K. **(f)** Log-log plots of $H_{\text{peak}}(\theta)$ originated from (d) and (e), where dotted lines are best-fits for γ extraction.

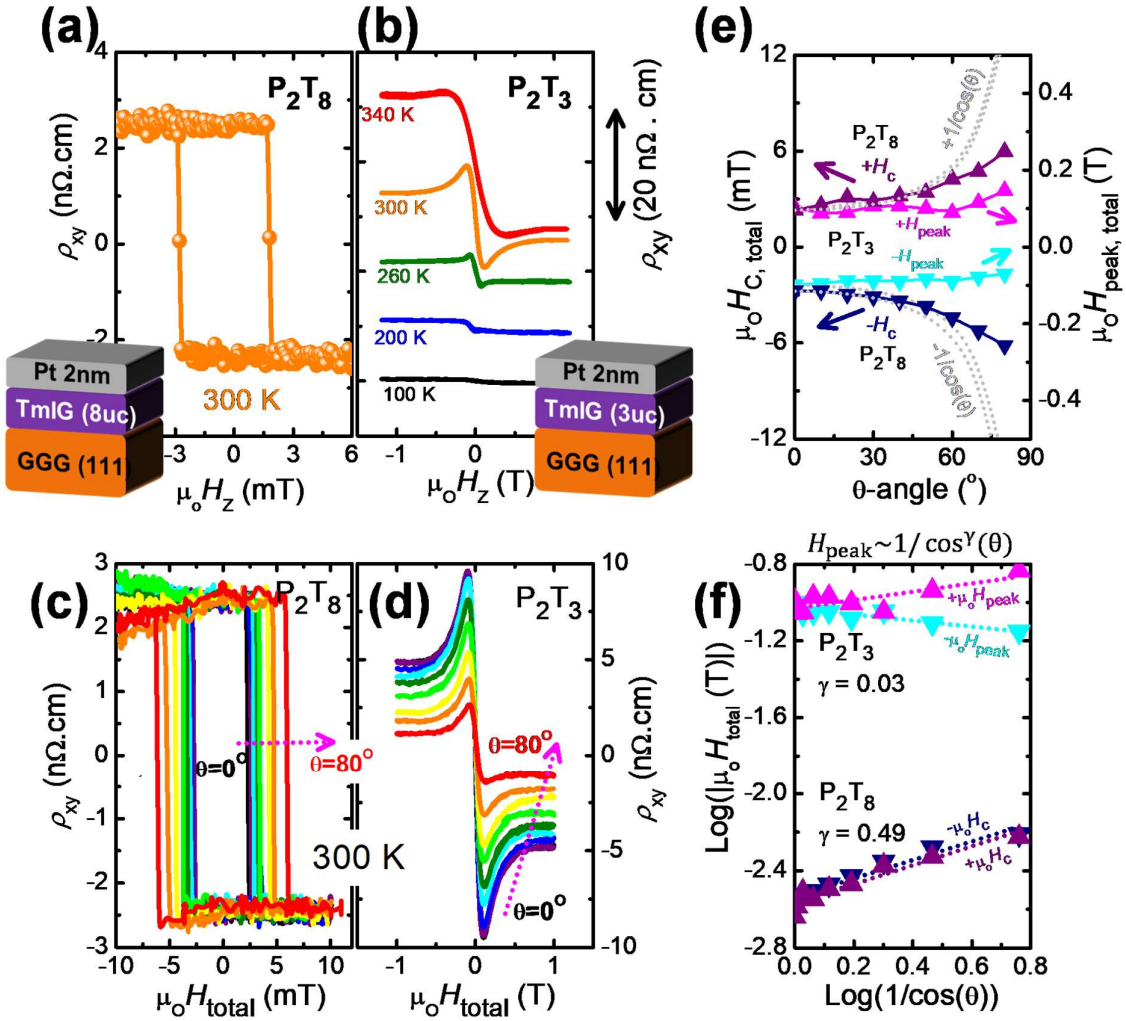

Figure 2: Pt-capped TmIG films on GGG(111) substrates with **(a)** 8uc (9.6nm) and **(b)** 3uc (3.6nm) TmIG, labelled as P_2T_8 and P_2T_3 respectively, for a consistent comparison with the SRO-based heterostructures (main text). $\rho_{xy}(H_{\text{total}}, \theta)$ data for **(c)** P_2T_8 and **(d)** P_2T_3 under the "total field rotation scheme". (**e**) Field-angle divergence plots and (**f**) Log-log plots for coercive fields of P_2T_8 and hump peak fields of P_2T_3. Dotted lines in (**e**) are the $1/\cos^1(\theta)$ trends as guide-for-the-eyes to illustrate the data curves have $\gamma<1$, while those in (**f**) are best fits for γ extraction.

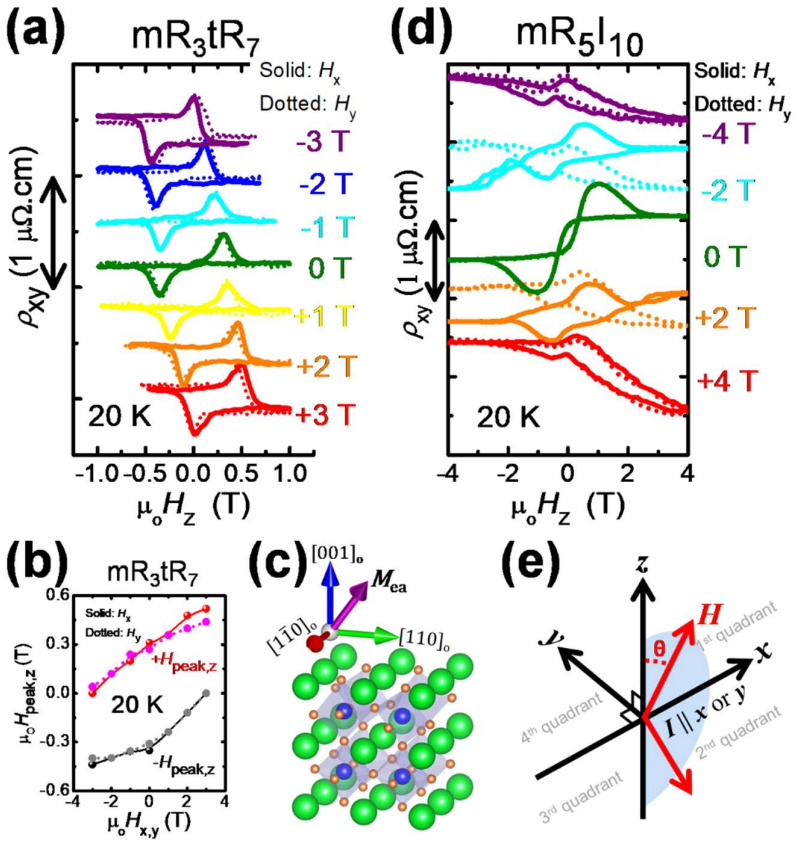

Figure 3: $\rho_{xy}(H_z, H_{x,y})$ data for **(a)** mR_3tR_7 and **(d)** mR_5I_{10}, with comparison between H_x (solid) and H_y (dotted) in-plane fields. Loops are vertically shifted for clarity. **(b)** Summary of z-component H_{peak} variations with $H_{x,y}$ in mR_3tR_7 from (a). A low current density $\boldsymbol{J}_{c,x}$ of $+6.24 \times 10^8$ A/m^2 was used for both heterostructures. **(c)** Inclined easy axis magnetization ($\boldsymbol{M}_{ea}$) of SRO thin film typically occurs on STO(001) substrate. **(e)** Schematic of the resolved field components $\rho_{xy}(H_z, H_{x,y})$ measurements by simultaneous variations of H_{total} and θ to maintain a particular $H_{x,y}$.

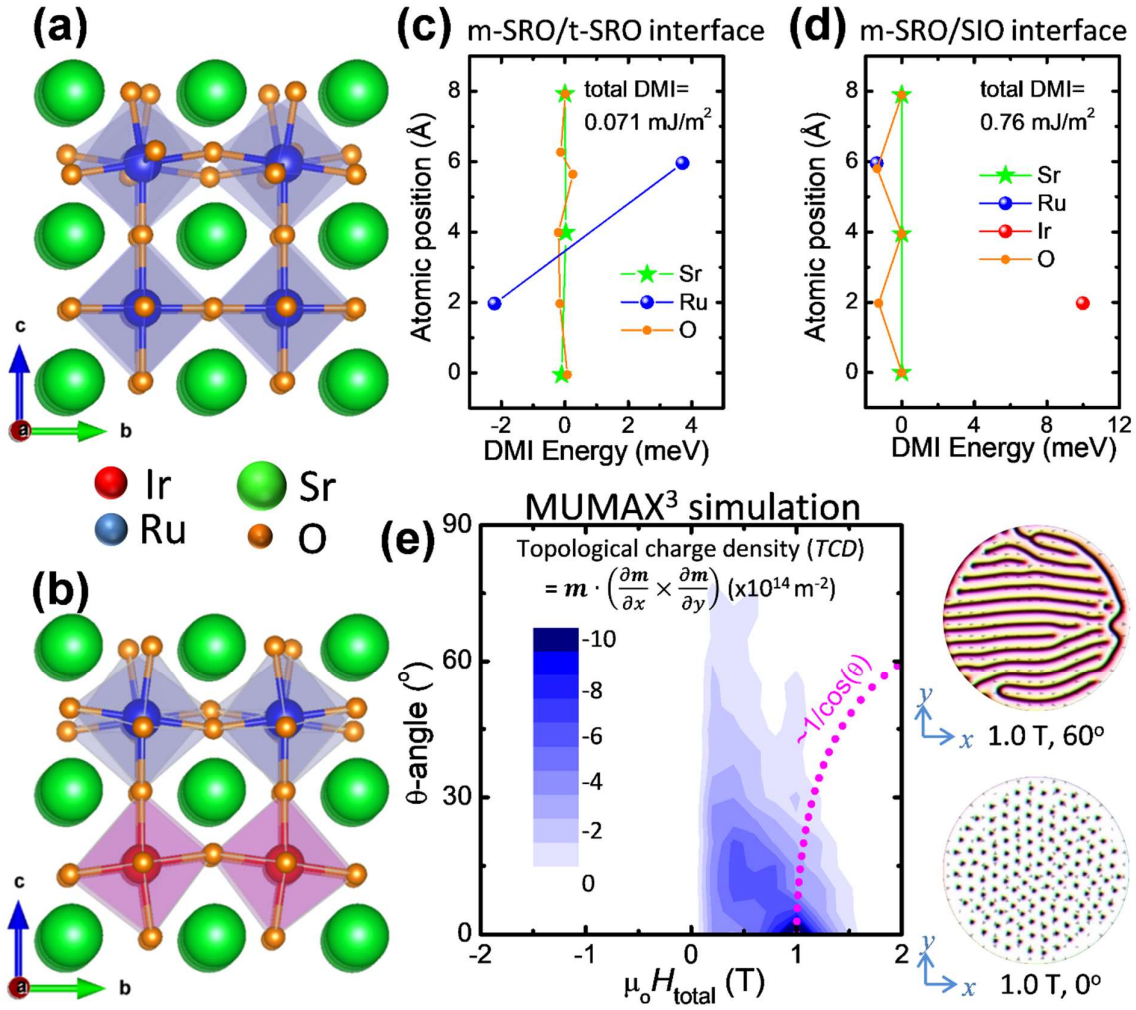

Figure 4: DFT structural models for **(a)** mR_3tR_7 and **(b)** mR_5I_{10} respectively. Layer and atomic species resolved DMI energies from DFT calculations for **(c)** mR_3tR_7 and **(d)** mR_5I_{10} respectively. **(e)** $TCD(H_{total},\theta)$ mapping obtained by MUMAX^3 using realistic parameters of mR_5I_{10}. Right panels: snapshots of magnetic textures extracted from the (H_{total},θ) states indicated.

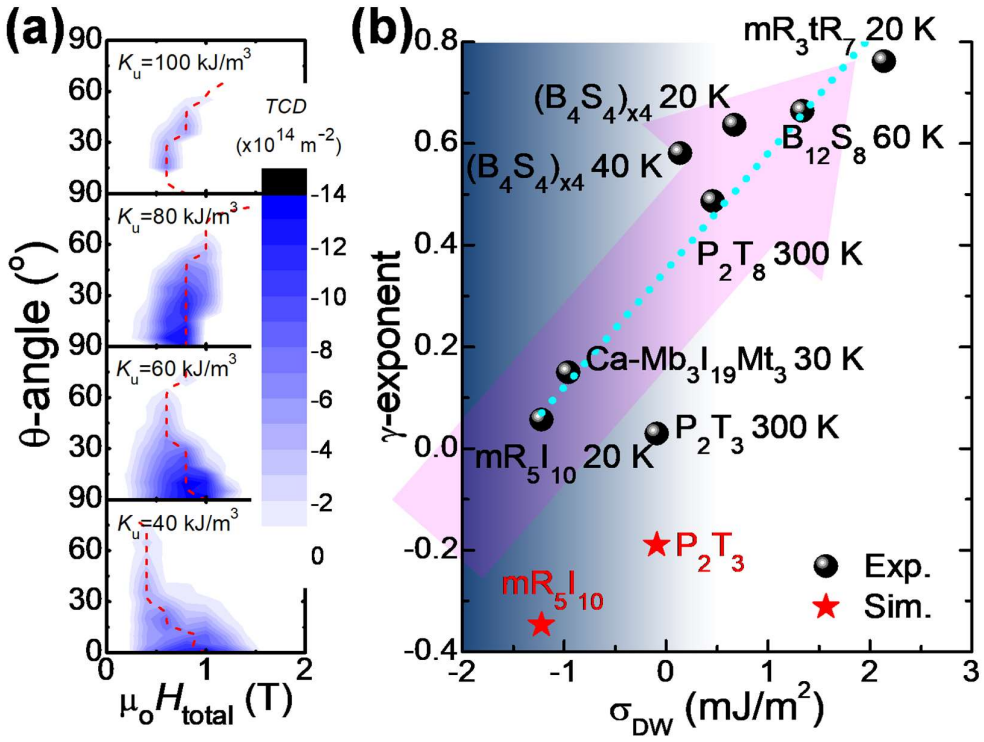

Figure 5: (a) *TCD*(H_{total},θ) mappings with varying K_u, with the *TCD* peak fields labelled by red dashed curves. **(b)** Trend of γ versus σ_{DW}, with parameters extracted from experiments (this work) and various references(*58, 62-64*). Details are given in supplementary table S2. The dotted line is the linear best fit.

SUPPLEMENTARY MATERIALS

Angular dependence of hump-shape Hall Effects for distinguishing between Karplus-Luttinger and Geometrical Origins

Additional Analyses on X-ray Diffraction

In Figure S1c, the half-integer XRD peaks of m-SRO and t-SRO thick films (34uc) are shown, with notations and HKL-indices following the Glazer's rules(*1, 2*). We believe that the broad humps around (0.5,1.5,1) are measurement artifacts. Considering that bulk m-SRO material is known to belong to the *pbnm* space group with $a^-a^-c^+$ tilt pattern, its in-phase (+) oxygen octahedral rotation axis should have shorter B-O-B bond length. Since the STO(001) substrate imposes an in-plane compressive strain to the film, it is energetically favourable for the in-phase rotation axis of m-SRO to align with the axes "*a*" or "*b*" under compression(*3*). Hence, $a^-a^-c^+$ is unlikely to occur in thin film cases before strain relaxation, while $a^-b^+c^-$ and $a^+b^-c^-$ may occur with equal probability(*3-5*). In our case, strong peaks HKL=(0.5,0.5,1.5) and (1.5,0.5,1.5), supports the existence of a^-. Then, a peak occuring at (0.5,0,1.5) supports b^+ and rules out b^-, hence c^- can be deduced from (0.5, 1.5,1.5), forming $a^-b^+c^-$. In t-SRO(34uc), most peaks are suppressed, consistent to tetragonal $a^0a^0c^0$ whch is also partially stabilized by oxygen vacancies(*6*). Similarly, almost all Half-integer XRD peaks are suppressed in mR_3tR_7 due to the dominant t-SRO. Hence, the interface is assigned as SRO($a^-b^+c^0$)/SRO($a^0b^0c^0$) as a reasonable approximation for subsequent DFT calculations.

For mR_5I_{10}, the SIO film was deliberately designed to be thick enough for relaxation from strain and tilt-suppression by the cubic STO(001) substrates, hence the a^+ and b^+ tilts are likely to form in SIO at regions away from the substrate. The peak at (0,0.5,1.5) thus belongs to the a^+ of the SIO film (red curve of Figure S1c) at region near the SRO/SIO interface, and can be assigned as $a^+b^0c^0$. Subsequently, the top SRO can be expected to have

weak $a^-b^+c^0$, bearing much resemblance to the thick m-SRO (34uc) with $a^-b^+c^-$. Previously in reference (*7*), we have discussed that the thick enough bottom SIO with relaxation from $a^0b^0c^0$ to $a^+b^0c^0$ is crucial to achieve the Hall-humps. Replacing the bottom SIO with a low pressure grown one with the same thickness will again result in total suppression in almost all half-interger XRD peaks, since oxygen vacancies in SIO also tend to stabilize tetragonal crystal structure, leading to suppression of Hall-humps. We believe the c^+ peaks at (0.5,1.5,1.0) visible in m-SRO(34uc), t-SRO(34uc) and mR_3tR_7 are resulted from further strain relaxation near the sample/air surface recovering its bulk-like *Pbnm* state of $a^-a^-c^+$, but are far away from and not relevant to the crucial interfaces responsible for DMI highlighted in main text Figure 3a,b.

Additional Data for Damping-like SOT of P_2T_8

In Figure S3a,b, P_2T_8 also exhibited an additional symmetric loop-narrowing effect ($\pm H_{C,z}$ reduction) at the small regimes of $\mu_o|H_x|<5$ mT. This effect can be understood from purely magnetic field torque acting on $\pm M_z$ domains causing easier switching for both polarities and is irrelevant to damping-like SOT on m_{DW}. Damping-like SOT becomes more relevant at $\mu_o|H_x|>5$ mT, since larger H_x may enhance the effect of damping-like SOT even at small $J_{c,x}<10^{10}$ A/m^2. Such symmetrical H_z loop-narrowing regime at low $\pm H_x$ was also observed but less frequently in different samples of mR_3tR_7. Hence, trivial magnetic bubbles can be inferred to be dominant in mR_3tR_7 with abundant DWs, while P_2T_8 is closer to abrupt single collinear M_z domain switching.

First-principle Calculations

In Density Functional Theory (DFT) calculations for Dzyaloshinskii-Moriya Interaction (DMI), we limited the structure in each case to a two-unit cell thin slab for optimal computational cost (main text Figure 3a,b). Before relaxation, the in-plane lattice

parameters *a* and *b* are fixed at 3.9053 Å following the substrate, while the out-of-plane lattice parameters *c* = 4.04 Å for t-SRO and 3.94 Å for m-SRO in mR_3tR_7. Likewise in mR_5I_{10}, the lattice parameters are *a*=*b*=3.9053 Å, while *c* = 3.95 Å for SIO and 3.94 Å for mSRO. Next, the WIEN2k package(*8, 9*) was employed in three steps (*10*). Firstly, structural relaxations were performed on top of the input obtained from half-integer HKL XRD until the forces became smaller than 0.01 eV/Å for determining the most stable interfacial geometries, resulting in small adjustments from the input. Secondly, the Kohn-Sham equations were solved using the generalized Bloch theorem(*11*) as implemented in non-collinear spin version of WIEN2k (WIENNCM) to generate wavefunctions of spin spiral state. An arbitrary spiral vector q of 0.1x2π/a* was chosen, where a*=2a is the in-plane lattice constant of the supercell needed to account for the octahedral rotation. Finally, a condition for the generalized Bloch theorem to be valid is that spin is isotropic and this precludes the inclusion of spin-orbit interactions. Thus to recover spin-orbit effects, we employ first-order perturbation for the spin-orbit Hamiltonian with wavefunctions obtained for the spin spiral to obtain the spin-orbit energy(*12*). This energy is then divided by the system volume and set to Dq to obtain the value of total DMI (main text Figure 3c,d).

Interestingly, the mR_3tR_7 sample is found to be unstable in DFT, consistent to experimental observation. When mR_3tR_7 was relaxed following the protocol of "forces <0.01 eV/Å" mentioned, the octahedral rotation angle across the interface became vanishingly small. In experiments, we observed a gradual evolution of all mR_3tR_7 samples from showing the Hall-humps (main text Figure 1a) into a single positive AHE square loop (hump vanished) within the course of 3-4 days if the sample is stored under ambient condition. This can be understood where the top 3uc m-SRO becomes progressively dominated by the bottom 7uc t-SRO layer at room temperature due to oxygen vacancy diffusion across the interface or atomic position shifting. Hence, all the subsequent magnetic field rotation analyses are

measured immediately after fresh sample growth, while the low measurement temperature (20 K) is capable of slowing down the evolution. Hence, in DFT, the DMI calculation of mR_3tR_7 was done without structural relaxation, and represents a metastable state. This is in contrast to mR_5I_{10} where the full structural relaxation did not produce significant change to the initial model built from half-integer XRD, while in experiment the Hall-humps of mR_5I_{10} is stable over several years.

Magnetometry and MUMAX^3 Micromagnetic Simulations

In Fig. S5a-d, the magnetometry data of mR_3tR_7, mR_5I_{10}, $B1_2S_8$, $(B_4S_4)_{x4}$-SL are shown. The *M*-*H* loops with *H*||z (out-of-plane) and *H*||x,y (in-plane) at the left panels are useful to calculate magnetic anisotropy and inference of saturation magnetization (M_{sat}) at various teemperatures. The Curie temperatures (T_C) can be inferred from the moment versus temperature (*M*-*T*) from the right panels. The field-cooling (FC) *M*-*T* curves of Figure S4b extending to higher temperature cut-offs (~150 K) than the zero-field-cooled (ZFC) *M*-*T* curves are likely due to the proximity-induced magnetism and spin-liquid behaviour of SIO film. These information are used as MUMAX^3 simulation, using the following equations:

$$A_{\mathrm{ex}} = \frac{3k_{\mathrm{B}}T_{\mathrm{c}}}{2j(j+1)a}$$

$$l_{\mathrm{ex}} = \sqrt{\frac{2A_{\mathrm{ex}}}{\mu_{\mathrm{o}}{M_{\mathrm{sat}}}^2}}$$

$$K_{\mathrm{u}} = \int_0^{H_{\mathrm{sat}}} (M_{\boldsymbol{H}||\boldsymbol{c}} - M_{\boldsymbol{H}||\boldsymbol{a}}) \cdot dH$$

where A_{ex}, j, a, l_{ex} and K_u are the exchange stiffness, total angular momentum quantum number per formula unit, lattice parameter, exchange length and uniaxial magnetic anisotropy respectively. Since Ru^{4+} ($4d^4$) is lying between the weak SOC (l-s coupling) and strong SOC

(j-j coupling) regimes with spin and orbital angular momentum of S=1, L=1, the SRO has j=1 because the two vectors are neither parallel nor antiparallel. While j=5/2 is typically suitable for Fe^{3+} ($3d^5$) with S=5/2 and L=0 in TmIG.

For SRO-based heterostructures, relatively low temperatures were chosen for K_u calculations as indicated in the *M-H* curves to match the fact that the DMI values extracted from DFT are ground state (0 K) values, and we do not know the trend of DMI reduction with thermal fluctuation. This strategy facilitates getting a good trend in main text Figure 4b. Due to presence of Ir^{4+} paramagnetic species in mR_5I_{10}, the M_{sat} data obtained from SQUID would be slightly less accurate. Hence, we allowed M_{sat} as the only free variable for manual optimization to match the TCD peak field to the peak of Hall-hump data at $\mu_o H_{peak}$=1.0 T and θ=0, before simulations of other θ-angles. Likewise, due to the difficulty in measuring precise magnetometry data for TmIG thin films grown on highly-paramagnetic GGG(111) substrates, K_u of P_2T_8 were extracted from reference (*13*) showing anisotropy field, H_K = 1460 Oe, and $K_u \approx \mu_o M_{sat} H_K$ =13140 J/m^3 while M_{sat} = 90 emu/cm^3 = 9x10^4 A/m. Whereas T_C of P_2T_8 and P_2T_3 can be confidently estimated to be 550 K and 300 K respectively, since 550 K is known to be the bulk value of garnet ferrites(*14*). Whereas from the supplementary Figure S2b we can see a divergence of Hall-hump (THE) in P_2T_3 around 300 K, consistent to the power-law scaling of $\rho_{xy}^{T} \propto |T - T_C|^{-\gamma'}$ discussed in reference (*15*), verifying its lower 2nd-order phase transition temperature. A simulation grid cell size of 4 nm < l_{ex} was used for all cases, with 256x256 meshes in the xy-plane but 1-cell in the z-direction thickness. The backward/forward field sweep simulations are always initialized with m=Uniform(0,0,±1) to retain the history of magnetization saturation. Each simulation was terminated after reaching a criterion of max-torque < 5x10^{-3}. The simulation parameters for mR_5I_{10} and P_2T_3 are shown in the table S1 below, resulting in hysteretic *TCD* in mR_5I_{10} but non-hysteretic TCD in P_2T_3.

	T_C	j	a	A_{ex}	M_{sat}	K_U	D_{int}	l_{ex}	Thickness	a_G
Unit	K		Å	pJ/m	kA/m	kJ/m^3	mJ/m^2	nm	nm	
mR_5I_{10}	125	1	3.93	3.43	63	24.8	0.76	36.3	1.97	0.1
P_2T_3	300	5/2	12.3	0.58	20	1	0.1	47.9	3.70	0.03

Supplementary Table S1: MUMAX^3 Simulation parameters of mR_5I_{10} and P_2T_3 for $TCD(H_{total},\theta)$ mappings.

Figure 4b in the main text was generated from the following data of table S2. K_u and D of P_2T_8 were extracted from (*13*) and (*16*), Ca-$Mb_3I_{19}Mt_3$ from (*17*), while K_U, A_{ex} and D of $B_{12}S_8$ use values of $B_{20}S_5$ from reference (*18*), since its magnetometry signal is too weak to be measured accurately from our SQUID-VSM setup. The rest of parameter values were experimentally determined in this work.

Samples	$\boldsymbol{K_U}$ (kJ/m^3)	$\boldsymbol{A_{ex}}$ (pJ/m)	$\boldsymbol{D}$ (mJ/m^2)	$\boldsymbol{M_{sat}}$ (kA/m)	$\boldsymbol{K_{eff}}$ (kJ/m^3)	$\boldsymbol{\sigma_{DW}}$ (mJ/m^2)	$\boldsymbol{\gamma}$
mR_5I_{10}	24.8	3.43	0.76	61.9	27.2	-1.17	0.057
mR_5I_{10} (sim.)	24.8	3.43	0.76	61.9	27.2	-1.17	-0.35
P_2T_3	1	5.76	0.06	115	9.31	1.04	0.029
P_2T_3 (sim.)	1	5.76	0.06	30	1.565	-0.07	-0.19
Ca-$Mb_3I_{19}Mt_3$	6.54	1.23	0.42	153	21.3	-0.67	0.15
$B_{12}S_8$ (60 K)	146	2.3	0.84	61.7	148	0.21	0.51
$(B_4S_4)_{x4}$ (20 K)	200.2	3.4	0.84	102.3	206.8	0.72	0.64
$(B_4S_4)_{x4}$ (40 K)	70.8	3.4	0.58	89.36	75.8	0.21	0.58
mR_3tR_7	107.9	3.2	0.071	135.8	119.4	2.26	0.76
P_2T_8	13.14	1.07	5.2×10^{-3}	100	19.4	0.56	0.49

Supplementary Table S2: Data list for the Figure 4b's plot.

SUPPLEMENTARY REFERENCES

1. A. M. Glazer, The classification of tilted octahedra in perovskites. *AcCrB* **28**, 3384-3392 (1972).
2. A. M. Glazer, Simple ways of determining perovskite structures. *AcCrA* **31**, 756-762 (1975).
3. T. C. van Thiel, J. Fowlie, C. Autieri, N. Manca, M. Šiškins, D. Afanasiev, S. Gariglio, A. D. Caviglia, Coupling Lattice Instabilities Across the Interface in Ultrathin Oxide Heterostructures. *ACS Materials Letters* **2**, 389-394 (2020).
4. Y. F. Nie, P. D. C. King, C. H. Kim, M. Uchida, H. I. Wei, B. D. Faeth, J. P. Ruf, J. P. C. Ruff, L. Xie, X. Pan, C. J. Fennie, D. G. Schlom, K. M. Shen, Interplay of Spin-Orbit Interactions, Dimensionality, and Octahedral Rotations in Semimetallic $SrIrO_3$. *Phys. Rev. Lett.* **114**, 016401 (2015).
5. P. Schütz, D. Di Sante, L. Dudy, J. Gabel, M. Stübinger, M. Kamp, Y. Huang, M. Capone, M. A. Husanu, V. N. Strocov, G. Sangiovanni, M. Sing, R. Claessen, Dimensionality-Driven Metal-Insulator Transition in Spin-Orbit-Coupled $SrIrO_3$. *Phys. Rev. Lett.* **119**, 256404 (2017).
6. W. Lu, P. Yang, W. D. Song, G. M. Chow, J. S. Chen, Control of oxygen octahedral rotations and physical properties in $SrRuO_3$ films. *Phys. Rev. B* **88**, 214115 (2013).
7. A. K. H. K. Zhi Shiuh Lim, Zhou Zhou, Ganesh Ji Omar, Ping Yang, Robert Laskowski, Ariando Ariando, Oxygen Octahedral Tilt Controlled Topological Hall Effect in Epitaxial and Freestanding SrRuO3/SrIrO3 Heterostructures. *arXiv:2204.06174*, (2022).
8. R. Laskowski, G. K. H. Madsen, P. Blaha, K. Schwarz, Magnetic structure and electric-field gradients of uranium dioxide: An ab initio study. *Physical Review B* **69**, 140408 (2004).
9. P. Blaha, K. Schwarz, F. Tran, R. Laskowski, G. K. H. Madsen, L. D. Marks, WIEN2k: An APW+lo program for calculating the properties of solids. *The Journal of Chemical Physics* **152**, 074101 (2020).
10. H. Yang, A. Thiaville, S. Rohart, A. Fert, M. Chshiev, Anatomy of Dzyaloshinskii-Moriya Interaction at Co/Pt Interfaces. *Phys. Rev. Lett.* **115**, 267210 (2015).
11. L. M. Sandratskii, Noncollinear magnetism in itinerant-electron systems: Theory and applications. *Advances in Physics* **47**, 91-160 (1998).
12. M. Heide, G. Bihlmayer, S. Blügel, Describing Dzyaloshinskii–Moriya spirals from first principles. *Physica B: Condensed Matter* **404**, 2678-2683 (2009).
13. C. Tang, P. Sellappan, Y. Liu, Y. Xu, J. E. Garay, J. Shi, Anomalous Hall hysteresis in $Tm_3Fe_5O_{12}$/Pt with strain-induced perpendicular magnetic anisotropy. *Phys. Rev. B* **94**, 140403 (2016).
14. R. Pauthenet, Spontaneous Magnetization of Some Garnet Ferrites and the Aluminum Substituted Garnet Ferrites. **29**, 253-255 (1958).
15. M. Raju, A. P. Petrović, A. Yagil, K. S. Denisov, N. K. Duong, B. Göbel, E. Şaşıoğlu, O. M. Auslaender, I. Mertig, I. V. Rozhansky, C. Panagopoulos, Colossal topological Hall effect at the transition between isolated and lattice-phase interfacial skyrmions. *Nat. Commun.* **12**, 2758 (2021).
16. L. Caretta, E. Rosenberg, F. Büttner, T. Fakhrul, P. Gargiani, M. Valvidares, Z. Chen, P. Reddy, D. A. Muller, C. A. Ross, G. S. D. Beach, Interfacial Dzyaloshinskii-Moriya interaction arising from rare-earth orbital magnetism in insulating magnetic oxides. *Nat. Commun.* **11**, 1090 (2020).

17. Z. S. Lim, C. Li, Z. Huang, X. Chi, J. Zhou, S. Zeng, G. J. Omar, Y. P. Feng, A. Rusydi, S. J. Pennycook, T. Venkatesan, A. Ariando, Emergent Topological Hall Effect at a Charge-Transfer Interface. *Small* **16**, 2004683 (2020).
18. L. Wang, Q. Feng, Y. Kim, R. Kim, K. H. Lee, S. D. Pollard, Y. J. Shin, H. Zhou, W. Peng, D. Lee, W. Meng, H. Yang, J. H. Han, M. Kim, Q. Lu, T. W. Noh, Ferroelectrically tunable magnetic skyrmions in ultrathin oxide heterostructures. *Nat. Mater.* **17**, 1087-1094 (2018).

SUPPLEMENTARY FIGURES

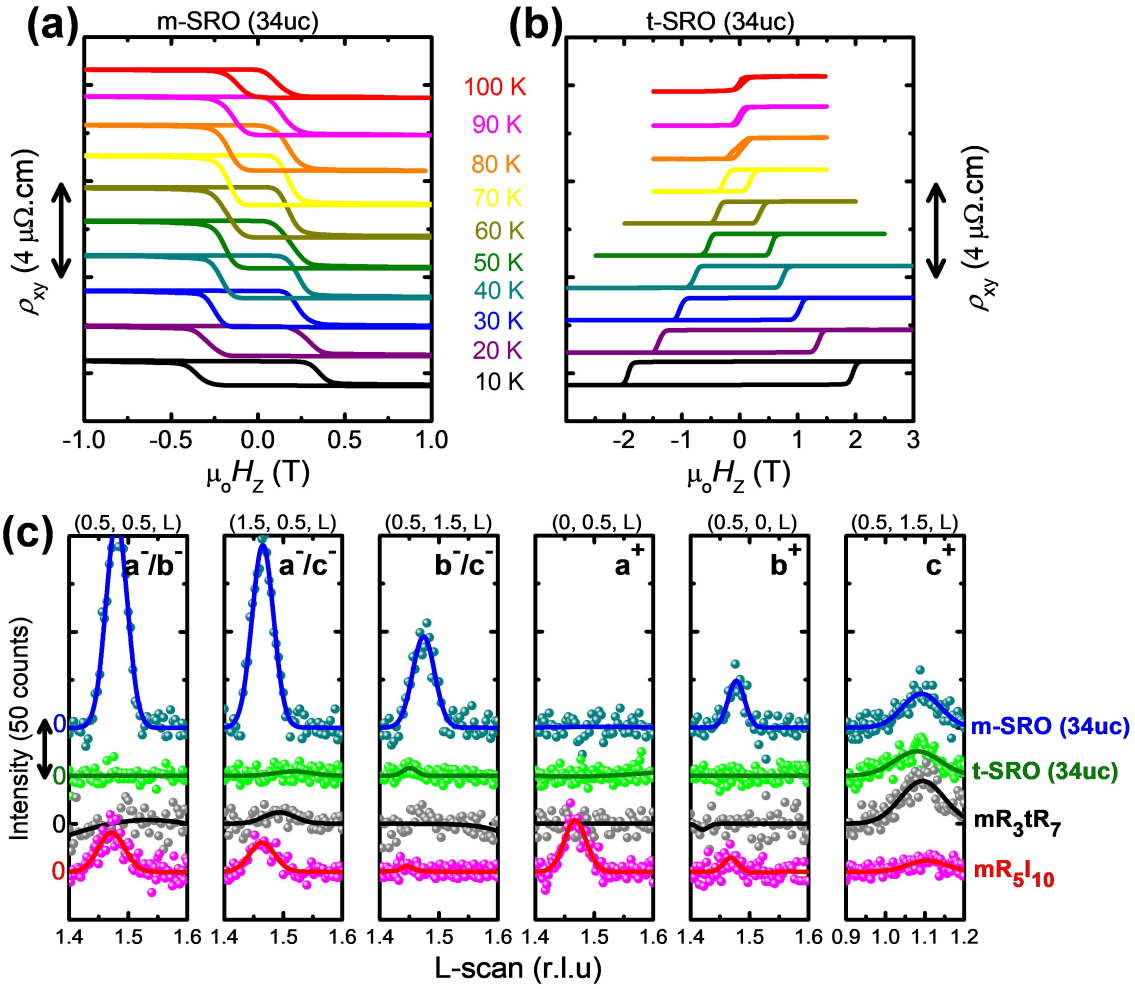

Supplementary Figure S1: KL-AHE loops of **(a)** m-phase SRO and **(b)** t-phase SRO thick films (34uc each) on STO(001) substrates without Hall-humps. Data of different temperatures are vertically shifted for clarity. **(b)** Half-integer X-ray Bragg diffraction data for thick films of m-SRO and t-SRO, mR_3tR_7 and mR_5I_{10}.

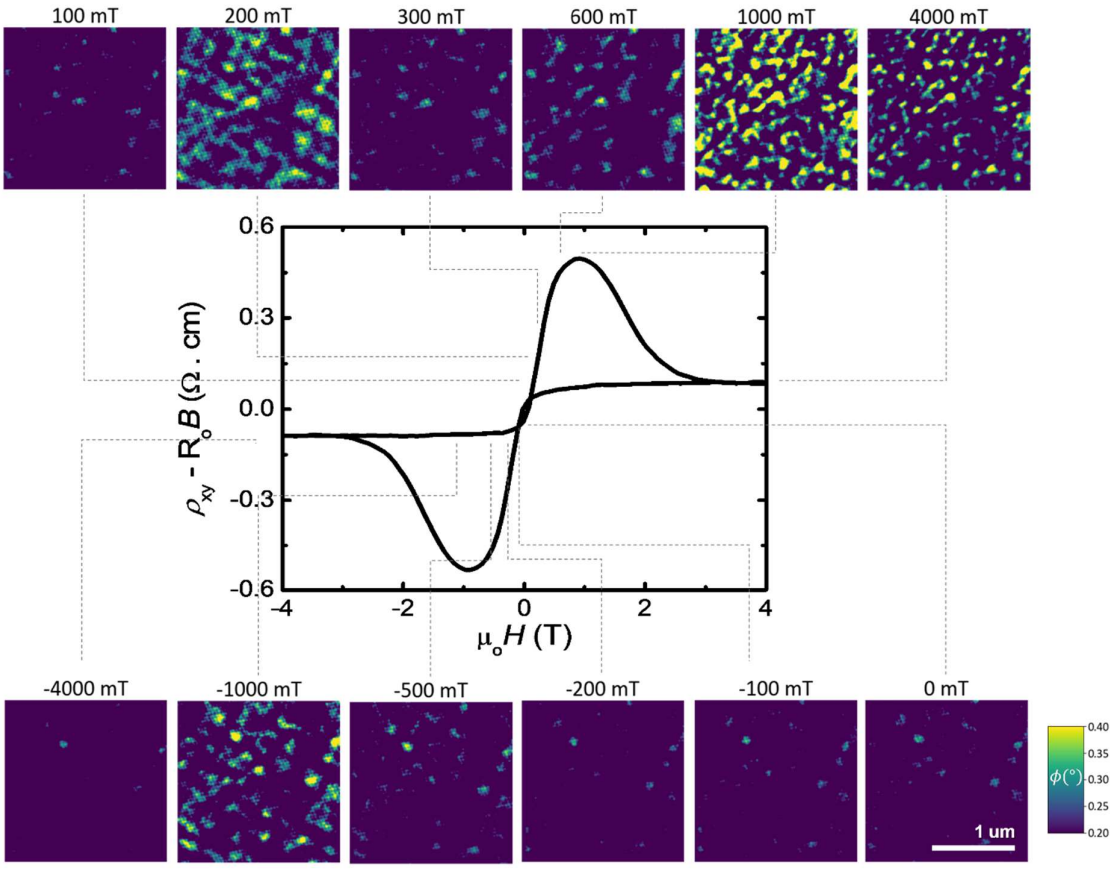

Supplementary Figure S2: Magnetic Force Microscopy (MFM) Δf-imaging data on mR_5I_{10}. The magnetic field was swept from +4 Tesla to -4 Tesla, scanned at 20 K. The $\rho_{xy}(H_{\text{total}}, \theta = 0)$ at 20 K is inserted at the centre for comparison, where dotted lines indicate the corresponding images and Hall states.

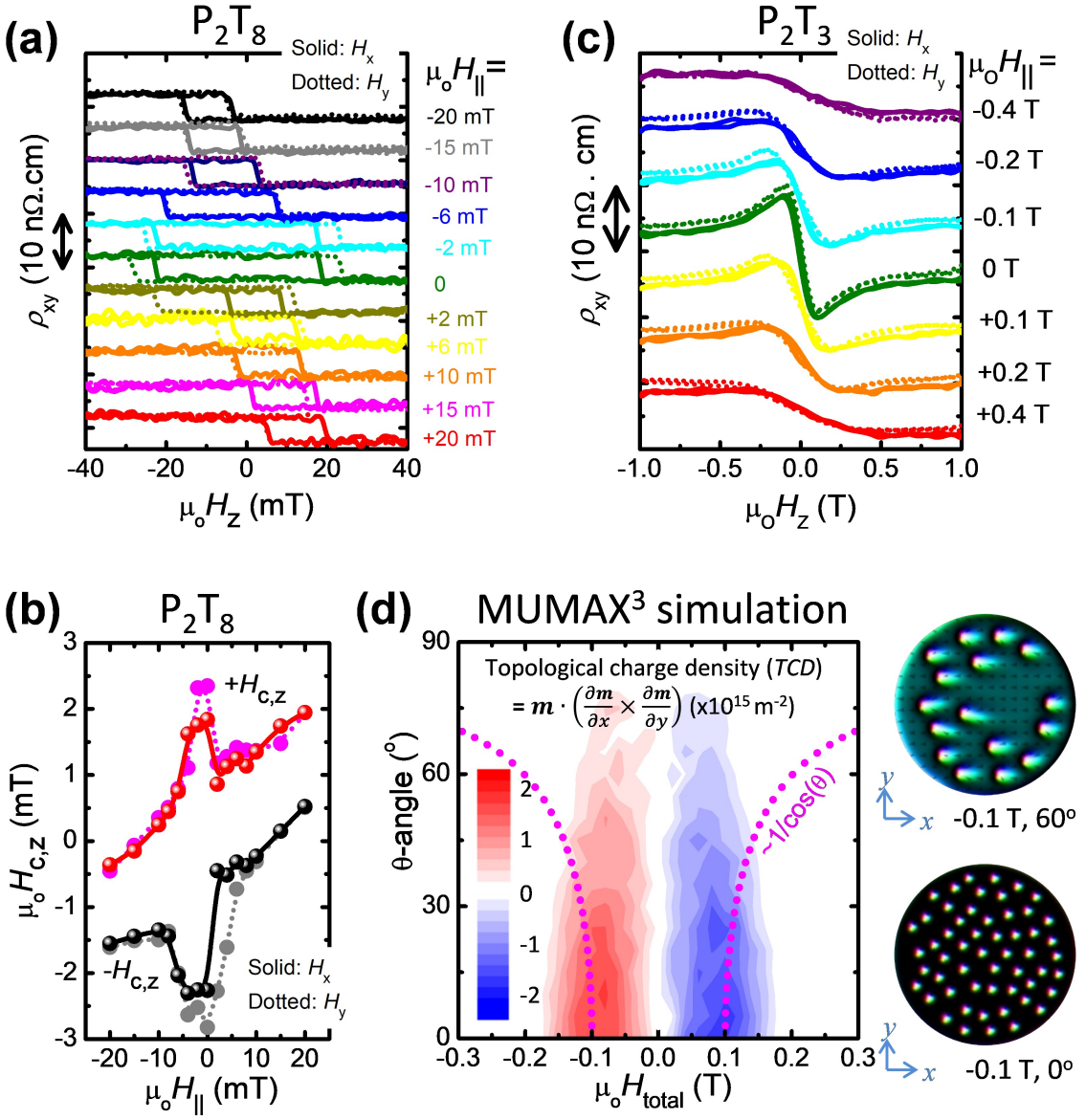

Supplementary Figure S3: $\rho_{xy}(H_z, H_{x,y})$ data for **(a)** P_2T_8 and **(c)** P_2T_3, with comparison between H_x (solid) and H_y (dotted) in-plane fields. Loops are vertically shifted for clarity. **(b)** Summary of z-component H_{peak} variations with $H_{x,y}$ in P_2T_8 from (a).. The charge current density $\boldsymbol{J}_{c,x}$ used was +7.5x10^9 A/m^2 for both P_2T_8 and P_2T_3. **(d)** $TCD(H_{total},\theta)$ mapping obtained by MUMAX^3 simulations done with parameters of P_2T_3, agreeing with its $\rho_{xy}(H_{total},\theta)$ data in Figure S2d. Right panels: snapshots of magnetic textures extracted from the (H_{total},θ) states indicated.

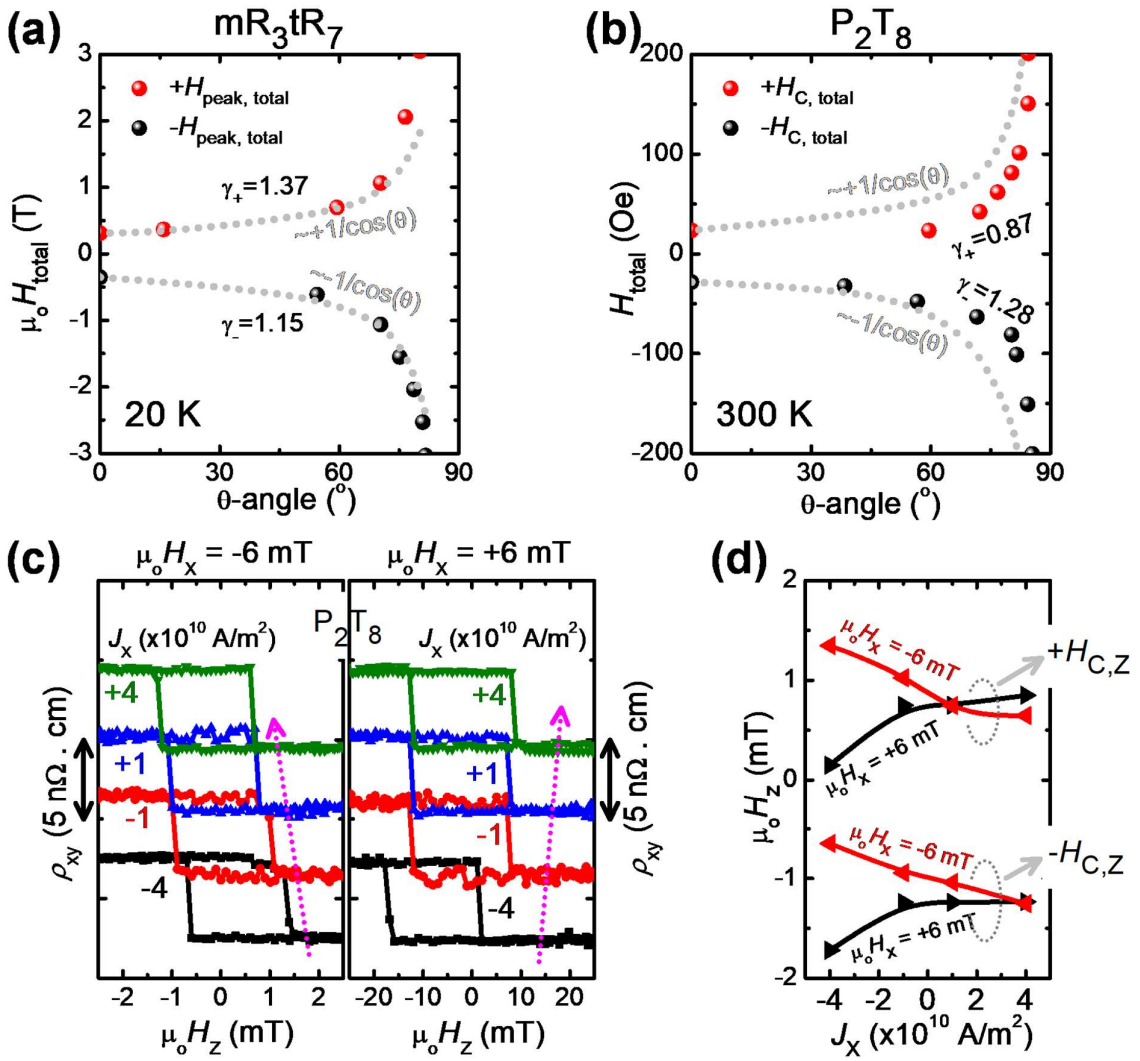

Supplementary Figure S4: The resulted θ-angle dependent $H_{peak,total}$ or $H_{C,total}$ trends after transforming the $H_{peak,z}$ and $H_{C,z}$ data from the resolved field-component scheme in main text Figure 3 for **(a)** mR_3tR_7 and **(b)** P_2T_8. The γ-exponents for the positive and negative branches are labelled. In P_2T_8, no sign of reduction/shrinkage can be seen in $H_{C,total}$ with increasing θ, although reduction in $H_{C,z}$ with increasing H_x is observed at small H_x. **(c)** ρ_{xy} versus H_z Hall-loops at constant H_x = ±60 Oe but with varying J_x from -4x10^{10} to +4x10^{10} A/m^2 showing clear shifts, with the z-component coercive fields ($H_{c,z}$) plotted in **(d)**. The shifting direction reverses upon reversing the sign of H_x is a clear signature of SOT effect.

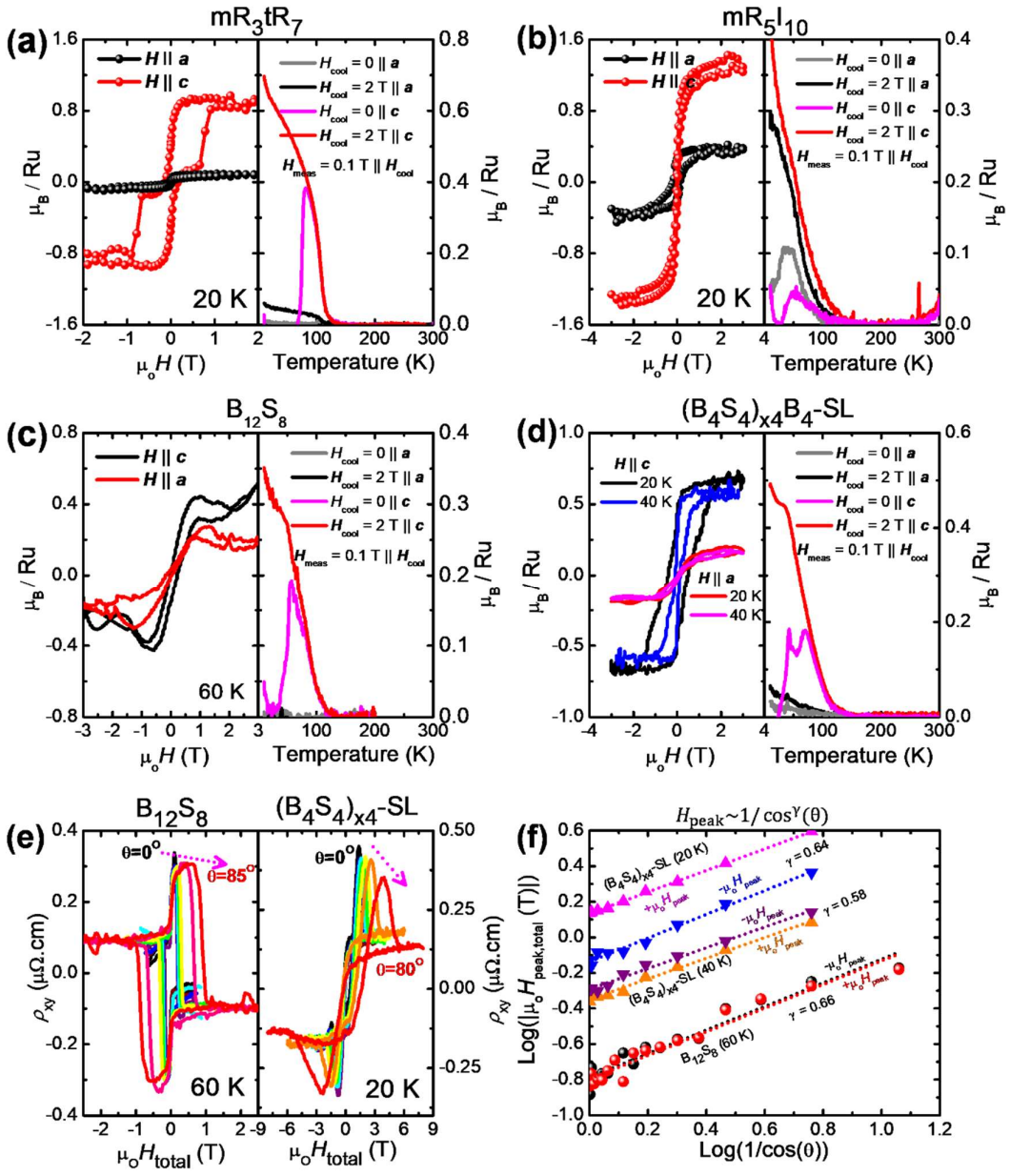

Supplementary Figure S5: Magnetometry data for **(a)** mR_3tR_7 **(b)** mR_5I_{10} **(c)** $B_{12}S_8$ and **(d)** $(B_4S_4)_{x4}$-SL respectively. In each heterostructure, the *M-H* curves for in-plane and out-of-plane fields are plotted on the left panels for calculations of K_U at the temperature indicated, while *M-T* are plotted on the right panels for calculation of A_{ex} from extracted T_C. **(e)** Hall-loops with increasing θ-angle in the total-field rotation scheme for $B_{12}S_8$ at 10 K (left) and $(B_4S_4)_{x4}$-SL at 20 K (right). **(f)** Log-log plots for γ extractions for various heterostructures after linear fittings (dotted lines).